Probing spatial properties of electronic excitation in water after interaction with temporally shaped femtosecond laser pulses: Experiments and simulations

Thomas Winkler [a], Cristian Sarpe [a], Nikolai Jelzow [a], Lasse H. Lillevang [b], Nadine Götte [a], Bastian Zielinski [a], Peter Balling [b], Arne Senftleben [a], Thomas Baumert [a],*

[a] Institute of Physics and CINSaT, University of Kassel, Heinrich-Plett-Str. 40, D-34132 Kassel, Germany
[b] Department of Physics and Astronomy, Aarhus University, Ny Munkegade 120, DK-8000 Aarhus C, Denmark

ABSTRACT

In this work, laser excitation of water under ambient conditions is investigated by radially resolved common-path spectral interferometry. Water, as a sample system for dielectric materials, is excited by ultrashort bandwidth-limited and temporally asymmetric shaped femtosecond laser pulses, where the latter start with an intense main pulse followed by a decaying pulse sequence, i.e. a temporal Airy pulse. Spectral interference in an imaging geometry allows measurements of the transient optical properties integrated along the propagation through the sample but radially resolved with respect to the transverse beam profile. Since the optical properties reflect the dynamics of the free-electron plasma, such measurements reveal the spatial characteristics of the laser excitation. We conclude that temporally asymmetric shaped laser pulses are a promising tool for high-precision laser material processing, as they reduce the transverse area of excitation, but increase the excitation inside the material along the beam propagation.

© 2015 Elsevier B.V. All rights reserved.

1. Introduction

Laser-based material processing with ultrashort laser pulses is a promising field that has emerged over the last decades [1] and is one of the key technologies for a variety of applications ranging from micro- and nanoprocessing of dielectric materials for photonic applications to medical and biological research. The main advantage is the increased precision of laser ablation due to a strongly reduced heat-affected zone. Moreover, it is possible to push the limits of the processing precision by using, for example, temporal [2,3] or spatial pulse-shaping techniques [4,5]. By employing temporally asymmetric shaped laser pulses, the lateral size of ablation structures in fused silica has been reduced by an order of magnitude below the diffraction limit [6,7]. Similar results have been found in a recent investigation, where these pulse shapes were used to process sapphire [8]. These structures may find applications in optoelectronic devices [9]. Even on soft matter, like polymers, these temporal pulse shapes have been used for downsizing purposes

[10]. In addition to solid transparent dielectrics, water has been the focus of a variety of studies with the background of medical and biological applications as for example in the field of eye surgery [11,12], cell-perforation [13–15] or dental healthcare [16].

In our previous study [17], we investigated the intensity and time dependent dynamics of the laser excitation in the spatial center of the pump pulse, which allowed us to understand why different temporal pulse shapes lead to different thresholds of laser-induced optical breakdown in water. Furthermore, we were able to observe that the measured change of the optical properties was higher for shaped than for unshaped laser pulses. This was a first indication that shaped pulses may lead to a higher excitation inside the sample compared to ultrashort bandwidth-limited laser pulses. In our previous investigation we focused on the temporal dynamics within the first picoseconds after the laser excitation [17]. In this contribution, we present our results of the spatial characteristics of the electron plasma after laser excitation with temporally shaped femtosecond laser pulses. These measurements are realized by an improved version of our previously reported ultra-stable common-path pump-probe technique [17]. By measuring the changes in the optical properties of our excited target material along a line transversely through the beam profile, the radial dependence

can be extracted. Since the excitation of electrons is the initial step in laser-based material processing of dielectrics [18], we performed rate equation simulations of the laser excitation including absorption and reflection of the laser pulses to relate the measured change in the optical properties to a conduction-band electron density at the surface and inside the water jet.

2. Experiment, simulations and sample system

2.1. Radially resolved common-path spectral interference

In this section, we give a short overview of the basic measurement scheme and changes that have been made to our existing experimental setup to provide radial information. Furthermore, the physical quantities that are required for the evaluation of the measured data are presented.

Our measurement technique, that is shown in Fig. 1, is based on an ultra-stable common-path spectral interference setup, as presented and discussed in more detail in [17]. In order to measure the laser-induced excitation of the sample, the fundamental 785 nm beam is split into a pump and probe arm. In the probe path, that passes a high precision motorized delay stage, the beam is frequency doubled in a α-BBO crystal and pre-compressed in a prism compressor [17]. Afterwards the 392 nm pulse is split into a pair of pulses in a 12.5 mm thick birefringent α-BBO crystal (in Fig. 1 α-BBO1). The two pulses, having a temporal distance of 6.5 ps and a FWHM pulse duration of 43 fs, are focused together with the temporally shaped fundamental 785 mm pump pulse of 35 fs onto the surface of a free flowing water jet, using a long working distance microscope objective (Mitutoyo M Plan APO 2×). The planar water jet is produced by a polished stainless steel nozzle and measured in situ to have a thickness of 121.3 ± 0.5 µm. The uncertainty of the water jets thickness is the statistical error for several measurements at the same position on the water jet, where the experiments were performed. The temporal shaping of the pump pulse is realized in our liquid crystal modulator-based home-build pulse shaper [19]. By using a motorized half wave plate (HW) together with the polarizer in the pulse shaper, the pump pulse power is adjusted.

The $1/e^2$ beam waists of the laser pulses was measured in the focus to be 24 µm for the pump and 35 µm for the probe pulse by imaging the pulses with a 40× magnifying system onto a CCD camera. The imaging system consists of a 20× long distance microscope objective (Mitutoyo M Plan APO 20×) and a 400 mm focusing lens.

In the measurements, first, the reference pulse propagates through the water jet, influenced by the optical properties of the unexcited water. Second, the pump pulse creates free electrons along its propagation direction, leading to a change in the optical properties, which are then probed by the subsequent 392 nm pulse. In order to ensure a very good overlap between pump and probe pulses, a part of the probe beam is led to a CCD camera using a pellicle beamsplitter (PBS). After the sample, the fundamental 785 nm beam is blocked out by a short pass filter (SP). The temporal delay between the reference and probe pulses is reduced to 0.2 ps by another 12.2 mm thick α-BBO crystal (in Fig. 1 α-BBO 2) and they are imaged by a microscope objective and a 400 mm focusing lens onto the entrance slit of a spectrometer (Princeton Instruments 320 spectrometer with a cooled CCD array). The cooled CCD array has dimensions of 1024×128 pixels, where the 1024-pixel-direction corresponds to the spectral resolution and 128 pixel-direction is used for the spatial recording. The spectral interference is thus recorded along a vertical cut through the probe pulse – selected by the entrance slit of the spectrometer. From the observed shift of the interference pattern, the changes of the optical properties – phase shift and optical density – can be extracted [17].

2.1.1. Optical properties of laser excited dielectrics relevant for data evaluation

The optical properties are defined by the dielectric function $\varepsilon(\omega)$ of the material, which is in the present investigation described by the Lorentz–Drude-Model for light with an angular frequency ω [20]:

$$\varepsilon(\omega) = \varepsilon_b - \frac{\omega_{\mathrm{pl}}^2}{\omega^2 + i\frac{\omega}{\tau}} \tag{1}$$

with the contribution of the valence electrons ε_b. The second part of Eq. (1) takes into account the contribution by "free" conduction
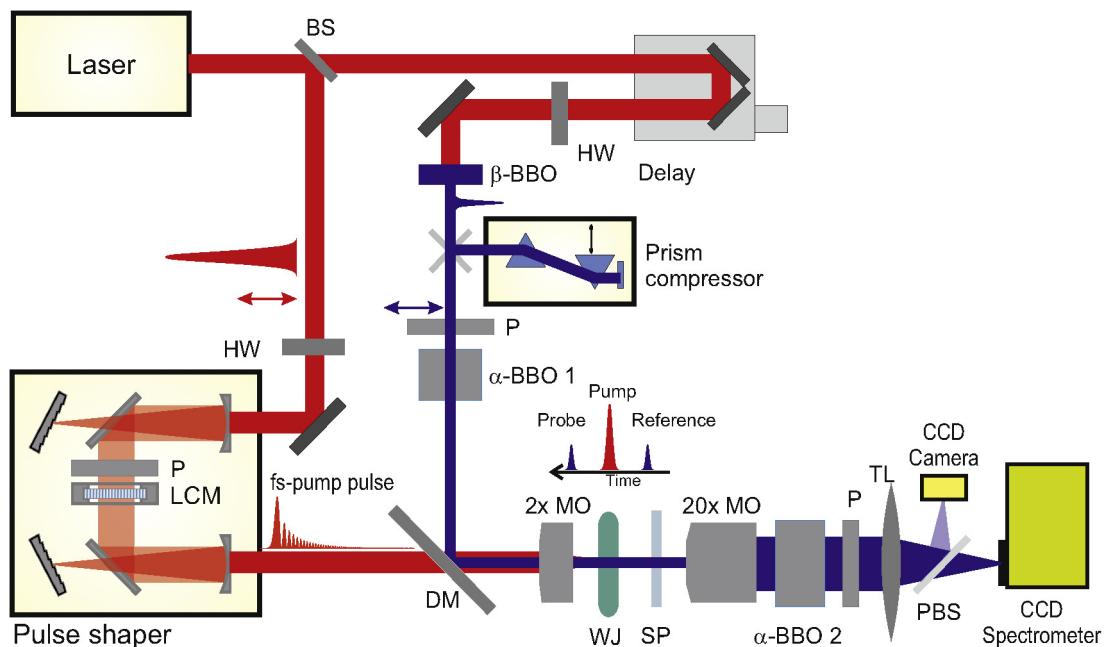

Fig. 1. Experimental setup – description in the text: BS – beamsplitter. HW – half waveplate, P – polarizer, LCM – liquid crystal modulator. DM – dichroic mirror, MO – microscope objective, WJ – free flowing planar water jet, SP – short pass filter, TL – tube lens, PBS – pellicle beamsplitter.

band electrons, dependent on the plasma frequency $\omega_{\text{pl}} = \sqrt{N_e e^2 / \varepsilon_0 m}$ and the electron scattering time τ. N_e is the conduction band electron density, $m = m_e/2$ is the reduced electron mass [21] and e the elementary charge, with its vacuum mass m_e.

The complex index of refraction for a dielectric material (with the magnetic permeability $\mu = 1$) is given by:

$$\tilde{n} = \sqrt{\varepsilon(\omega)} \qquad (2)$$

The measured refractive index change $\Delta\tilde{n}$ between probe and reference pulse due to the conduction band electron density is given by [17]:

$$\Delta\tilde{n}(N_e) = \tilde{n}(N_e) - \tilde{n}(N_e = 0) = -\frac{1}{2n_0}\left(\frac{\omega_{\text{pl}}}{\omega}\right)^2 \frac{1}{1 - 1/i\omega\tau} \qquad (3)$$

The resulting change of the complex refractive leads to a lower real part of the refractive index for the probe pulse and therefore to a higher phase velocity of the light in the water jet. This results in a decreased temporal delay between the probe and reference pulse, which is measured as a phase shift $\Delta\Phi$ in the spectral interference [17,22,23] depending on the free electron density:

$$\Delta\Phi = \frac{2\pi}{\lambda}\int_0^L Re(\Delta\tilde{n})dz = -\int_0^L \frac{\pi \cdot \omega_{\text{pl}}^2}{\lambda \cdot n_0 \left(\omega^2 + \frac{1}{\tau^2}\right)}dz \qquad (4)$$

where L is the sample thickness and λ is the probe wavelength of 392 nm.

Due to the excitation of free electrons, the imaginary part in Eq. (3) is nonzero, causing absorption, measured as optical density:

$$\begin{aligned} \text{OD} &= -\ln(T) = -\frac{4\pi}{\lambda}\int_0^L Im(\Delta\tilde{n})dz \\ &= \int_0^L \frac{2\pi \cdot \omega_{\text{pl}}^2}{\lambda \cdot n_0 \cdot \omega \cdot \tau^2 \left(\omega^2 + \frac{1}{\tau^2}\right)}dz \end{aligned} \qquad (5)$$

The absorption by free electrons also affects the pump pulse as it is propagating through the sample in z-direction, leading to a non-homogenous excitation of the sample. As Eqs. (4) and (5) show, the spectral interference reflects the integrated phase shift and optical density accumulated over the whole sample thickness. In the case of very high excitation, i.e. if a significant amount of the valence band electrons are excited, the dielectric constant ε_b of the material decreases. This can be incorporated in Eq. (3) by using the Clausius–Mossotti relation [18,23] for the bound dielectric "constant" ε_b.

In order to reveal the spatial properties of the laser excitation, we performed single shot fluence dependent measurements using ultrashort bandwidth-limited as well as temporally asymmetrically shaped pump laser pulses. For pulse shaping we used our home-built liquid-crystal-modulator-based device [19]. The resulting changes in the optical properties, i.e. the phase shift, were evaluated for each radial position of the laser beam providing information about the radial dependence on the laser excitation. Due to the slightly elliptic shape of the pump pulse, the beam waist of the selected radial component is smaller (21 μm) than the average beam waist (24 μm). For recording and evaluation of the data, the same radial positions for both pulse shapes were chosen. The measurements are performed at pump-probe delay times, where only the contribution by the free electrons are observed and the measurements are not influenced by the optical Kerr effect [17]; this is at 3 ps for the temporally shaped and at 0.3 ps for the bandwidth limited laser pulse, respectively.

2.2. Simulations

We present now the rate equation model used to calculate the laser excitation by the temporal pulse shapes, as well as the resulting changes to the optical properties for a direct comparison with the measurements. The simulations are based on a simple generic rate equation model to calculate the time dependent conduction band electron density as presented in a variety of works [11,17,21,24–28]. We take into account the excitation of electrons from the valence into the conduction band via multiphoton and avalanche ionization, respectively. To keep our model as simple as possible, we only include multiphoton ionization with six photons. An increase in the order of the process caused by the ponderomotive shift of the band-gap energy at high intensities is not included. In addition, the ionization coefficients, σ_6 and α, for the multiphoton and avalanche ionization, are kept constant and used as fitting parameters as described in [17]. In the present data set we obtained 1.4×10^{-47} cm^9/W^6 s with an error of $\pm 20\%$ for σ_6 and 2.8 cm^2/W s $\pm 50\%$ for α. All simulations shown are performed in an intensity regime where tunnel ionization can be neglected.

The time-dependent conduction band electron density $N_e(t)$ is given by:

$$\frac{dN_e(t)}{dt} = (N_{\text{Max}} - N_e)/N_{\text{Max}} \cdot (\sigma_6 I(t)^6 + \alpha \cdot I(t) \cdot N_e(t_{\text{ret}})) \qquad (6)$$

with $I(t)$ the temporal pump pulse intensity distribution, t is the current time and t_{ret} the retardation time. N_{Max} is the valence band electron density of the unexcited water, estimated by taking into account one electron for each water molecule with the molecular mass of 18 and a density of 1 g/cm^3 is thus given by 3.3×10^{22} 1/cm^3. We use the retardation time t_{ret} first introduced by Vogel and coworkers in [11] and also employed in our previous studies [17] in order to take into account the scattering processes in the inverse Bremsstrahlung process, which leads to a natural retardation of the avalanche ionization process. The retardation time is a simple approximation of the time a conduction band electron requires to reach the critical energy for impact ionization, which is according to [11] $E_{\text{Crit}} = 1.5 \cdot E_{\text{Gap}}$, with the band gap energy E_{Gap}. A more elaborate model, taking into account the conduction band dynamics is the multiple rate equation model introduced by Rethfeld et al. [29] and extended by Christensen et al. [30]. To realize the more simple approach, we couple the laser field at time t with the electron density that was present at the earlier time $t_{\text{ret}} = t - n \cdot \tau$, where n is the number of photons that are required to reach the critical energy for impact ionization. In our case of 785 nm laser pulses with a photon energy of $E_{\hbar\omega} = 1.58$ eV we obtain for $n = 1.5 E_{\text{Gap}}/E_{\hbar\omega} = 8$. τ is the electron scattering time, which was set to a constant value of $\tau' = 1.6$ fs to calculate the retardation [17] but explicitly taken into account for the optical properties (see below).

The reflection coefficient at the front air–water interface is calculated by Fresnel-equations at normal incident [20]:

$$R(N_e) = \left|\frac{n_1 - \tilde{n}_{\text{Water}}(N_e)}{n_1 + \tilde{n}_{\text{Water}}(N_e)}\right|^2 \qquad (7)$$

with the linear refractive index of the ambient material (air) $n_1 = 1$ and the refractive index of the excited water jet given by Eqs. (1) and (2):

$$\tilde{n}_{\text{Water}}(N_e) = \sqrt{n_{\text{H}_2\text{O}}^2 - \frac{\omega_{\text{pl}}^2}{\omega^2 + i\frac{\omega}{\tau}}} \qquad (8)$$

with the refractive index of the unperturbed water $n_{\text{H}_2\text{O}}$ (1.329 at 785 nm and 1.339 at 392 nm [31]).

The scattering time τ, which is the reciprocal of the scattering rate, consists of a constant term for the electron–phonon scattering and an electron-density dependent term [32,33], which can be written as:

$$\frac{1}{\tau} = \frac{1}{\tau_{ep}} + \frac{1}{(\tau^* N_{Crit}/N_e)} \tag{6}$$

$1/\tau_{ep}$ is the constant electron–phonon scattering rate, where $\tau_{ep} = 1.6\,\text{fs}$ [17]. τ^* is the scattering time coefficient that sets the scattering time for the case that the conduction band density reaches the critical electron density [32] N_{Crit}. The critical electron density is defined as the case when the laser lights angular frequency ω equals the plasma frequency ω_{pl}. The scattering time coefficient was used as a fitting parameter and chosen to $\tau^* = 0.2\,\text{fs}$, obtaining the best agreement between simulation and experiment. In a low excitation regime, where a constant excitation along the propagation direction of the laser pulse can be assumed, we found the electron density dependent term to be neglectable. However, at higher fluences it has to be taken into account for the simulation in order to reproduce the experimental results.

Taking into account the reflection of the pump pulse, the temporal intensity distribution, for the BWL laser pulse with a FWHM temporal duration Δt, incident to the first layer of the material is:

$$I(t, z = 0) = (1 - R(N_e)) \cdot I_0 \cdot \exp\left(-4\ln 2\left(\frac{t}{\Delta t}\right)^2\right) \tag{9}$$

which is used to calculate the excitation in this layer. I_0 is the peak intensity given by:

$I_0 = F_P/\Delta t$, with the peak fluence $F_P = 2\sqrt{4\ln 2/\pi} \cdot E/A_{Focal}$ (E – laser pulse energy, $A_{Focal} = \pi \cdot w_0^2$ focal area, w_0 – laser beam waist). The absorption in the excited layer is generally calculated by the following differential equation [34]:

$$\frac{\partial I(t, z)}{\partial z} = -6\hbar\omega\sigma_6 I^6(t, z) - \alpha' I(t, z) \tag{10}$$

with the absorption coefficient:

$$\alpha' = 2\omega/c \cdot Im[\tilde{n}_{Water}(N_e)] \tag{11}$$

The first part of Eq. (10) describes the absorption of light due to the multiphoton ionization, whereas the second part describes the inverse bremsstrahlung absorption by the free electrons via the conduction band electron density dependent absorption coefficient of the material α'. Since the contribution of absorption by multiphoton ionization is significantly lower compared to the free carrier absorption, it is not taken into account in our simulations to keep them as simple and fast as possible. The resulting intensity distribution is incident to the next layer of the material and the excitation of the material is calculated iteratively with a step size of one nm in depth. As the Rayleigh ranges of both pump ($2.3 \times 10^3\,\mu\text{m}$) and probe beam ($9.3 \times 10^3\,\mu\text{m}$) are much larger than the sample thickness ($0.121 \times 10^3\,\mu\text{m}$), it can be assumed that the sample is uniformly illuminated, thus having a constant beam waist w_0 over the whole sample thickness L. Therefore, the radial intensity distribution in the first layer of the sample is given by:

$$I(t, z = 0, r) = (1 - R(N_e)) \cdot I_0 \cdot \exp\left(-4\ln 2\left(\frac{t}{\Delta t}\right)^2\right)$$
$$\cdot \exp\left(\frac{-2r^2}{w_0^2}\right) \tag{12}$$

with the radial position r.

2.2.1. Temporal pulse shapes

The temporally asymmetric laser pulses were created via Fourier transform pulse shaping applying a third order spectral
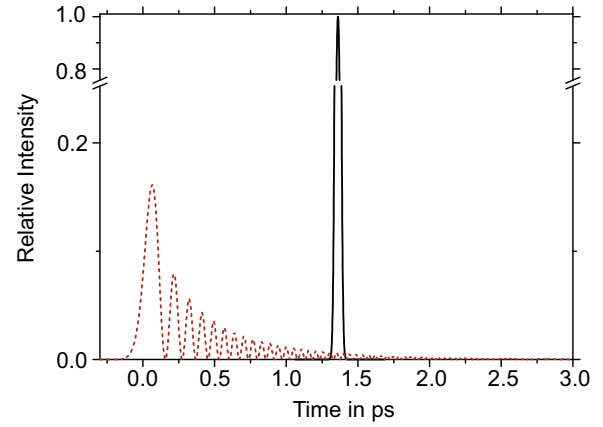
Fig. 2. Relative temporal intensity distribution for a 35 fs FWHM bandwidth-limited (black-solid line) and a third-order-dispersion shaped (red-dashed line) laser pulse with a TOD parameter $\phi_3 = 6 \times 10^5\,\text{fs}^3$ having identical fluence. The TOD shaped pulse resembles a squared and damped Airy function [43]. The BWL laser pulse is shifted in time for a better visualization. (For interpretation of the references to color in this figure legend, the reader is referred to the web version of this article.)

phase function (TOD) [35]: $\phi(\omega) = (\phi_3/3\,!)(\omega - \omega_0)^3$ with a value of $\phi_3 = 6 \times 10^5\,\text{fs}^3$ around the central angular frequency ω_0. The temporal pulse shapes used in our investigations are shown in Fig. 2 for identical fluence. The (maximum-)peak intensity is approx. 6 times higher for the BWL laser pulse as compared to the TOD shaped laser pulse.

2.3. Sample system

We use water as a model system for dielectric materials. It was shown that the excitation processes in liquid water are similar to those in solid dielectric materials, which allows useful information about the general excitation processes also for solid dielectrics to be extracted [17,36]. The band gap of water has been widely discussed over the last decades. The most commonly used value, 6.5 eV [11,37,38], has been questioned within the last years [21,39]. Recent experiments and simulations provided a more detailed view at the electronic properties of water, including different ionization and dissociation channels, indicating several excitation paths ranging from 6.5, 8.3 up to 9.3 eV [21,39]. In our work we take a fixed band gap of 8.3 eV [39,40], thus having a 6-photon photoionization process for 785 nm laser pulses. We use double distilled water in order to avoid contributions from impurities to the measured signals [11,21].

3. Experimental results, simulations and discussions

In the following, we present radially resolved phase shift measurements as a function of fluence of the pump pulse. We also compare the fluence dependence of the phase shift in the center ($r = 0\,\mu\text{m}$) with the one taken from a radial (fluence) line. In order to determine the spatial extent of the phase shift, we first evaluate the measured radial distribution at fluences where the phase shift in the central part is equal for BWL and TOD laser pulses. These excitation conditions are taken as input for rate equation simulations to compare simulated and measured phase shifts. Then we use the same conditions to calculate the conduction band electron density at the surface of the water jet and find a much lower electron density at the surface for TOD shaped pulses. Differences in the distribution of the surface electron density and the accumulated phase shift are revealed by discussing the depth dependent excitation at these excitation conditions. In order to relate our measurements and simulations to the goal of laser material
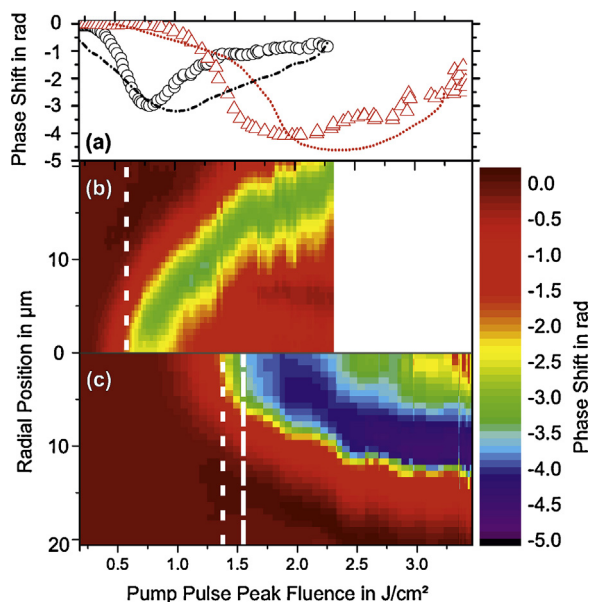
Fig. 3. (a) Pump pulse fluence dependence of the phase shift in the central part (BWL black circles, TOD red triangles) and extracted from the radial distribution at a fixed peak fluence of 2.25 J/cm² for the BWL (black dot-dashed line) and 3.25 J/cm² for the TOD laser pulse (red dotted line). (b) Radially resolved phase shift measurements as a function of pump-pulse-peak fluence for the BWL and (c) TOD shaped laser pulse. Dashed vertical lines in (b) and (c) indicate positions where the radially dependent phase shift data for Fig. 5 were extracted. (For interpretation of the references to color in this figure legend, the reader is referred to the web version of this article.)

processing, we simulate the depth and radially dependent electron density for the situation where the TOD has the same excitation at the surface as the BWL laser pulse. Finally, the measured and simulated radially dependent phase shift accumulated over the sample thickness and simulated radially dependent surface-electron densities are shown in the case of equal excitation at the surface.

3.1. Experimental results

3.1.1. Bandwidth-limited laser pulses

Fig. 3(a), as well as Fig. 4 shows the fluence dependence of the central part of the phase shift (black circles) for bandwidth limited laser pulses. The threshold fluence for excitation is reached around 0.2 J/cm², where the phase shift starts to decrease to its minimum value of around −3 rad (Fig. 3(a)). Reaching the maximum change of the phase shift is usually related to an excitation region for optical breakdown [17,41]. The observed power law scaling, extracted only from the central part of the pump pulse, in a regime of the phase shift between 0.1 and 1 rad is 6.2 ± 0.2, indicated by the black dotted lines in Fig. 4. This directly correlates to the estimated band gap
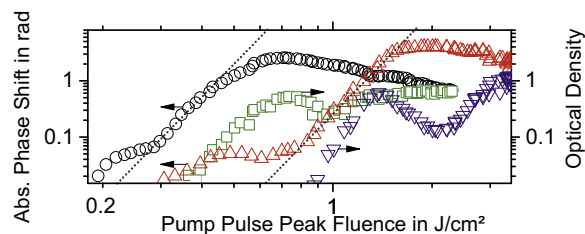
Fig. 4. Double-logarithmic representation of the measured absolute phase shift and optical density for BWL (circles and squares) and TOD shaped laser pulses (up and down pointed triangles) extracted from the central part in Fig. 3. The black dotted lines indicate a power law scaling of 6. Please note that the measured phase shift is negative. (For interpretation of the references to color in the text, the reader is referred to the web version of this article.)

of 8.3 eV. However, close to the detection limit of the experiment, between 0 and 0.01 rad, we measured an excitation of the sample with a lower order process than the main contribution (Fig. 4). This is in accordance with lower ionization mechanisms in water reported by Elles et al. [40] and Linz et al. [21]. As we only have a small amount of data points in this regime, we are not able to provide a power law scaling fit. Remarkable is that the excitation by this lower order process seems to saturate until the main excitation process sets in. Thus, we were able to observe a pump pulse fluence dependent transition from two distinct photo-ionization processes. The phase shift at which the first excitation saturates is around 0.05 rad, which correlates to an electron density of just $1.4 \times 10^{18} \mathrm{~cm}^{-3}$ assuming a constant electron density (Eq. (4) – with a constant scattering time of 1.6 fs) along the propagation direction of the laser pulse, which is valid in this regime [17]. Please note that this electron density is too low in order to provide a detectable change in the optical density.

With increasing fluence, the phase shift starts to increase again, visible as a bend of the slope in Fig. 3(a) [17]. The reason for this behavior is still unclear and was so far, not observed in any spectral- or spatial-interference experiments on solid dielectrics [25,26,42]. The increase of the phase shift might be related to the influence of the decreasing valence band electron contribution to the dielectric function, described via the Clausius–Mossotti relation [18] or due to avalanche cooling caused by interband collisions changing the scattering rate of the electron plasma. At this point, a more complex and detailed theoretical approach is required to understand these processes in the highly excited material, since our model is only valid in the excitation regime until the optical breakdown as will be shown in Section 3.2. Furthermore it can be seen that with increasing fluence, the decrease in phase shift moves toward greater radii following the spatial intensity profile of the pump pulse, shown in the radially resolved fluence dependent phase shift in Fig. 3(b). Pulse-to-pulse energy fluctuations do not influence the experiment, since single-shot measurements are performed and the energy of every pump pulse is monitored. The phase shift measurement is also not influenced by energy fluctuations, since probe and reference pulse energies change together, giving no change in phase or transmission [17].

In addition to the phase shift, the optical density (OD) was measured and the results for the central line are shown in Fig. 4 (green squares). As observed in our previous investigations [17], the onset of the OD is shifted toward higher fluence and follows then the same power law scaling as the phase shift, as expected from Eqs. (4) and (5). With increasing pump pulse fluence, the optical density undergoes a minimum, which was also reported in our previous investigations. Until now, this behavior was not observed elsewhere and its origin has still not been identified. Currently we investigate this behavior in more detail. From both, optical density and phase shift (Eqs. (4) and (5)), the electron scattering time was extracted as presented in [17] to be $\tau_{ep} = 1.5 \pm 0.4$ fs from the region in which both quantities are following the power law (0.1–0.9 rad phase shift). Here, we assume that the contribution to the scattering time by the electron density dependent part to be neglectable (see Section 2.2). This result is in a very good agreement to our previously reported value of 1.6 fs [17].

3.1.2. TOD shaped laser pulses

Pump-pulse-fluence dependent measurements are performed using positive TOD shaped femtosecond laser pulses. This temporally asymmetric pulse shape, as shown in Fig. 2, has a strong pulse followed by a train of sub pulses with decreasing intensity ending after around 3 ps, resembling a squared and damped Airy function [43]. The temporal pulse shape was characterized in the focus via cross correlation [17]. In Fig. 3(c) the radially resolved and pump-pulse-fluence dependent phase shifts are shown. The onset of the

phase shift decrease is shifted by a factor of around 2.2 toward higher fluences, as seen in our previous investigation [17]. This is caused by the drastically decreased peak intensity of the shaped pulse by a factor of around six, as seen in Fig. 2. As in the case of the BWL, in the center of the beam, shown in Fig. 3(a) and 4 (red triangles), the phase shift starts to decrease until a maximum change of around −4 rad, which is significantly higher than in the case of the BWL pulse (−3 rad). With increasing fluence, the phase shift starts to increase again. However, the increase is smaller as compared to the bandwidth-limited pulse.

In the phase shift range of 0.1–1 rad, the slope follows the same power law of 6.2 ± 0.2 as the BWL laser pulse, indicated by the black dotted line in Fig. 4. Even if this might be unintuitive since the TOD has a much higher pulse duration, close to the excitation threshold, multiphoton ionization is the driving process leading to the same power law. Furthermore, the lower order excitation process also appears for the shaped laser pulse. The onset of this process is only shifted by 1.5 times toward higher fluences and shows a saturation that persists for over 0.5 J/cm² before the main excitation process, following the power law of 6.2 ± 0.2, starts.

The measurement of the optical density for the TOD laser pulse shows the same behavior as the corresponding one for the BWL. In comparison, the optical density shows here a much more pronounced minimum, which occurs over a larger fluence regime for the shaped pulse.

3.1.3. Fluence dependence of the phase shift – center- vs. radial-line

Before we turn to a direct comparison of both pulse shapes, we compare the fluence dependence of the phase shift measured in the center with the phase shift obtained from the radial measurement. This is a valid comparison as at the highest fluence used in the experiments, a cut along the radial distribution of the pump pulse contains all fluences that are also contained in the central measurement (see Fig. 3(a) – signs). Thus, in a first approximation, both measurements should give identical results when mapped on the same fluence scale. In Fig. 3(a) the fluence dependent phase shift for the central line (signs) and for the radial cut (lines) at 2.25 J/cm² for the BWL and 3.25 J/cm² for the TOD are shown. The qualitative shape of the curves is similar, however, the radial distribution is less steep. This discrepancy may be attributed to linear- and nonlinear propagation effects that occur at higher fluences. Note that plasma-defocusing and Kerr-induced self-focusing can change the beam waist of the laser pulse in that regime, in principle [44–46]. However, even though in the present experiment the power for self-focusing is exceeded by more than one order of magnitude, the self-focusing length i.e. the length over which the beam collapses, is larger than the sample thickness [44]: to be specific, we consider the highest fluence used for the BWL laser pulse which is around 2.5 J/cm². Here, the applied power of 142 MW exceeds the critical power for self-focusing of water at 785 nm $P_{Crit} = 3.77\lambda^2/8\pi \cdot n_{H_2O} \cdot n_2 = 3.66$ MW, with a nonlinear refractive index of $n_2 = 1.9 \times 10^{-16}$ cm²/W [47], by nearly a factor of 40. Nevertheless the resulting self-focusing length [44] of 723 μm is nearly seven times larger than the sample thickness. For the TOD laser pulses the applied power is even lower due to the increased pulse duration.

Regarding the changes of the phase shift we also observe that the maximum change is higher for the radial cut with 10% more for BWL pulses and 20% more for TOD pulses. This may indicate that linear- and nonlinear propagation of the pump beam can lead to higher electron density inside the material. Besides the pump, also the probe pulse can be affected by plasma defocusing of a highly excited sample, causing a longer propagation through the sample, possibly accumulating a higher phase shift. This comparison shows the importance and the need for spatially resolved measurements
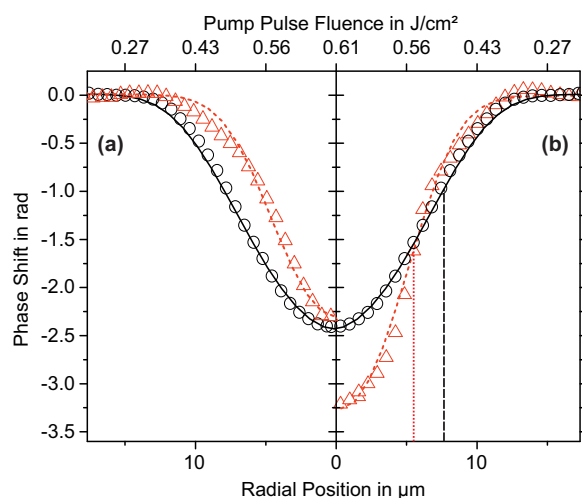

Fig. 5. Measured (symbols) and simulated (lines) radially dependent phase shift for BWL (black) and TOD (red) laser pulses: (a) equal *measured* phase shift at $r = 0$ μm for both pulse shapes. For the TOD shaped laser pulses the fluence is increased by a factor of 2.2. The data was extracted from the lines indicated in Fig. 3(b) for the BWL and Fig. 3(c) for the TOD (short dashed lines). (b) Equal *simulated* electron density at $r = 0$ μm for both pulse shapes. The fluence for TOD laser pulse is increased by a factor of 2.5 and the data was extracted from the lines indicated in Fig. 3(b) and Fig. 3(c) (long dashed line for TOD). Black dashed and red dotted vertical lines indicate the radius at which the phase shift decreased to half of the minimum value. (For interpretation of the references to color in this figure legend, the reader is referred to the web version of this article.)

of laser excitation of dielectric materials as the general behavior cannot simply be extracted from a single radial scan at high fluences. Furthermore, an enhanced numerical treatment, based on Schrödinger [46] or Maxwell's [48] equations is required in order to fully understand the experimental results. At low and moderate fluences, the radial dependence shows the same behavior as a central line scan. Simulation and experiment agree in this regime very well (see Fig. 5(a) and (b)) as will be discussed next.

3.2. Simulations and discussion

Now we address the comparison of the BWL and temporally shaped laser pulses. For a direct comparison of the radial properties of the laser excitation at a peak fluence of 0.61 J/cm² for the BWL pulse and 1.34 J/cm² for the TOD shaped pulse is chosen. Under these excitation conditions, an equal accumulated phase shift of around −2.3 in the center of the pump pulse at $r = 0$ μm is achieved. In Fig. 5(a) the radial distribution of the phase shift is shown. The white dashed lines in Fig. 3(b) and (c) indicate the fluence where the radial distribution was extracted. Both phase shift distributions reach a value of around −2.3 rad in the center, and both strongly decrease with increasing radius as expected from the beam profile of the pump pulse. However, the phase shift decreases much stronger in the case of the TOD shaped laser pulse as compared to the BWL laser pulse. It seems that the excitation takes place over a smaller area/radius for TOD shaped femtosecond laser pulses. As the measured phase shift, given by Eq. (4), is the integrated value over the whole sample thickness and represents not the excitation at the surface of the water jet, we performed rate equation simulations for a better understanding of the spatial excitation properties.

At first, we simulated the measured radially dependent phase shift after passing the water jet for both, BWL and positive TOD laser pulses using the same fluences as in the experiment. In Fig. 5(a) the resulting simulated and measured phase shift is shown. Simulated and measured values agree well. To reach the same phase shift in the central part for the TOD laser pulse, the required fluence is 2.2 times higher, in simulation and experiment. The simulation
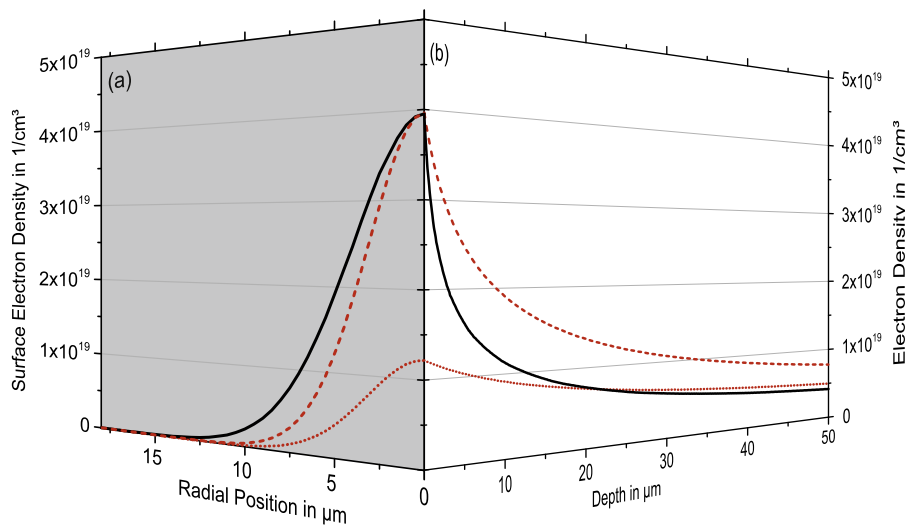
Fig. 6. Simulated radially- and depth-dependent phase shift for BWL (black) and TOD (red) laser pulses: (a) radially dependent phase shift for: equal phase shift at $r = 0\,\mu m$ (red dotted line), with the same fluence as in Fig. 5(a). Equal electron density at $r = 0\,\mu m$ (red dashed line), with the same fluence as in Fig. 5(b). (b) Depth-dependent conduction band electron density at the center of the laser pulse ($r = 0\,\mu m$) for the same cases as in (a). (For interpretation of the references to color in this figure legend and the text, the reader is referred to the web version of this article.)

reproduces the phase shift for all radial positions and thus all fluences. This validates our model that takes multiphoton and avalanche ionization into account as described above. In order to correlate the measured phase shift distribution with the actual excitation of the sample, we calculated the radial distribution of the electron density just at the surface ($L = 0\,\mu m$) of the water jet using the fluences that led to the $-2.3\,rad$ phase shift in the central part as shown in Fig. 5(a). In Fig. 6(a), the simulated radially dependent electron densities for BWL (black solid line) and TOD (red dotted line) pulses at the surface of the water jet are shown. Surprisingly, the observed differences between both pulse shapes are much higher as in the phase shift measurement: the maximum density, obtained by the TOD laser pulse, is about a factor of 4 below the maximum of the bandwidth-limited laser pulse. In addition, the excitation at the surface is more localized. The discrepancy between the measured phase shift and simulated excitation at the surface is clarified by the depth-dependent electron density, shown as the red dashed line for the TOD and the black solid line for the BWL laser pulses in Fig. 6(b). The electron density decreases for both pulse shapes with increasing depth. However, for the TOD laser pulse, the decrease is very low, such that from around 20 μm, the electron density is higher for the TOD laser pulse compared to the BWL. Thus, the probe pulse accumulates a higher phase shift over the rest of the sample, giving at the end the same values as for the BWL laser pulse. The reason for the behavior of the TOD laser pulse is discussed next in the context of results from material processing.

For (surface-)material processing as for example ablation or sustainable refractive index changes it is usually necessary that the electron density at the surface has to reach a certain value. In order to reach the same electron density at the surface for the TOD as the BWL laser pulse in our simulations, we had to increase the fluence of the TOD laser pulse by a factor of 2.5, as shown in Fig. 6(b). This factor was also observed in the processing of fused silica [6,7] and sapphire [6,8], where the threshold of ablation was shifted around 2.5× toward higher pulse energies for the TOD laser pulse. Furthermore, even in this and our previous investigations in water, the fluence difference for reaching the maximum phase shift – which is usually close to the optical breakdown [25] – was shifted by a factor of 2.5 toward higher pulse fluence for the TOD laser pulse. This indicates that the same processes as in solid dielectrics are addressed.

Now we come back to the difference between phase shift and surface excitation/electron density with an emphasis on the maximally reached phase shift being higher for the TOD laser pulses. To that end we discuss the simulated depth-dependent electron density for the central part at $r = 0\,\mu m$ of the laser pulses. We use the fluences where the same electron density is obtained at the surface for both pulse shapes. To be specific, a peak fluence of $0.61\,J/cm^2$ was used for the BWL pulse, whereas the fluence for the TOD laser pulse was 2.5× higher i.e. $1.52\,J/cm^2$. In Fig. 5(b) the depth-dependent electron density is shown for both pulse shapes. Starting from an equal electron density in the first layer, the electron density drastically decreases for both pulse shapes, but for the TOD laser pulse (red dashed line), the electron density decreases much less. This leads to a higher excitation inside the material and therefore a higher phase shift accumulated by the probe pulse. The reason for the higher excitation inside the material by the TOD laser pulse is related to the longer pulse duration and therefore the creation of free electrons mainly driven by avalanche ionization [17]. The strong pulse at the front of the TOD pulse train (Fig. 2) creates a relatively low free electron density via multiphoton ionization, whereas the rest of the pulse-train slowly increases the electron density to a much higher value [6,17]. This also leads to a slower increase of the absorption coefficient, which is proportional to the electron density (Eq. (11)), reaching its highest value when the lowest intensity of the pump pulse is present [17].

Finally, we compare the radial phase shift distribution in the discussed case of equal excitation at the surface. In Fig. 5(b) the radial-dependent simulated and measured phase shift – for $0.61\,J/cm^2$ (BWL) and $1.52\,J/cm^2$ (TOD) pump-pulse peak fluence is shown. Note that the phase shift in the central part is around 1.4 times higher for the TOD ($-3.2\,rad$) as compared to the BWL ($-2.3\,rad$). This factor is similar to the regime where the maximum phase shift is reached in the central part, as seen in Fig. 3(a). There the BWL pulse has a minimum at $-3\,rad$ and the TOD pulse at $-4\,rad$. This indicates that the spatial properties observed in the low and medium excitation regime may also be valid in the high excitation regime. The radial position of the phase shift, as it decreased to half of the maximum value, is smaller for the TOD shaped ($r = 5.5\,\mu m$) compared to the BWL ($r = 7.6\,\mu m$) laser pulse, indicated by the dashed (BWL) and short-dashed lines (TOD) in Fig. 5(b). In terms of area, the shaped pulse will excite about

half the area compared to the BWL laser pulse. The same relation between BWL and TOD laser pulses is found in the radial distribution of the conduction band electron density at the surface at the material, shown in Fig. 6(a). The results obtained in this study correlate to material processing results on fused silica [7] and sapphire [8], where the same temporal pulse shapes have been used. In both material systems, ablation structures created from bandwidth-limited laser pulses were relatively large and shallow, whereas the structures obtained by TOD shaped laser pulses were spatially more confined and much deeper. Although the current model does not quantitatively predict the very large differences in the observed radii of the generated structures in fused silica and sapphire, the observed trends in this investigation correlate well with the materials-processing results. Currently we plan radially resolved common-path spectral interference experiments on solid samples with the aim to demonstrate that the indications obtained on water are transferable to dielectrics i.e. to show directly that TOD shaped pulses lead to excitation over a smaller area, but larger depth, as compared to ultrashort BWL laser pulses.

We expect that other temporal pulse shapes may also lead to the observed behavior of reducing the area of excitation but increasing the depth. Especially picosecond or strongly chirped femtosecond laser pulses with the same pulse duration as the TOD laser pulse may result in similar features. However, these pulse shapes will require much more fluence compared to the TOD, as the symmetric laser intensity is only slowly increasing, making the TOD laser pulse with its asymmetric shape a much more efficient approach.

4. Conclusion

In conclusion, radially resolved, fluence-dependent pump-probe measurements on water were reported, using ultrashort BWL and positive TOD shaped femtosecond laser pulses. We showed that the measured excitation by TOD shaped laser pulses is confined to a drastically reduced area compared to BWL laser pulses by almost a factor of two. A rate equation model, including absorption and reflection of the pump pulse, reproduced the results. The simulations showed further that TOD shaped laser pulses lead to a higher electron density excitation deeper inside the material as compared to BWL laser pulses. We conclude that TOD shaped laser pulses can control the area and depth of laser excitation. This presents a powerful tool for high precision laser material processing.

Acknowledgements

References

[1] R.R. Gattass, E. Mazur, Nat. Photonics 2 (2008) 219–225.
[2] R. Stoian, M. Wollenhaupt, T. Baumert, I.V. Hertel, in: R. Hull, C. Jagadish, R.M. Osgood, J. Parisi, Z. Wang, H. Warlimont (Eds.), Laser Precision Microfabrication, Springer, 2010, pp. 121–144.
[3] N. Götte, T. Kusserow, T. Winkler, C. Sarpe, L. Englert, D. Otto, T. Meinl, Y. Khan, B. Zielinski, A. Senftleben, M. Wollenhaupt, H. Hillmer, T. Baumert, in: K. König (Ed.), Optically-Induced Nanostructures for Biomedical and Technical Applications, De Gruyter, Berlin [u.a.], 2015, pp. 47–72.
[4] I. Alexeev, K.-H. Leitz, M. Schmidt, Phys. Procedia 5 (2010) 533–540.
[5] F. Courvoisier, P.-A. Lacourt, M. Jacquot, M.K. Bhuyan, L. Furfaro, J.M. Dudley, Opt. Lett. 34 (2009) 3163–3165.
[6] L. Englert, B. Rethfeld, L. Haag, M. Wollenhaupt, C. Sarpe-Tudoran, T. Baumert, Opt. Express 15 (2007) 17855–17862.
[7] L. Englert, M. Wollenhaupt, C. Sarpe, D. Otto, T. Baumert, J. Laser Appl. 24 (2012) 042002-1–042002-5.
[8] J. Hernandez-Rueda, N. Götte, J. Siegel, M. Soccio, B. Zielinski, C. Sarpe, M. Wollenhaupt, T.A. Ezquerra, T. Baumert, J. Solis, ACS Appl. Mater. Interfaces 7 (2015) 6613–6619.
[9] T. Meinl, N. Götte, Y. Khan, T. Kusserow, C. Sarpe, J. Köhler, M. Wollenhaupt, A. Senftleben, T. Baumert, H. Hillmer, Proc. SPIE 9126 (2014), 91262B-1–91262B-10.
[10] E. Rebollar, J. Mildner, N. Götte, D. Otto, C. Sarpe, J. Köhler, M. Wollenhaupt, T. Baumert, M. Castillejo, E. Rebollar, J. Mildner, N. Götte, D. Otto, C. Sarpe, J. Köhler, M. Wollenhaupt, T. Baumert, M. Castillejo, Appl. Surf. Sci. 302 (2014) 231–235.
[11] A. Vogel, J. Noack, G. Hüttman, G. Paltauf, Appl. Phys. B 81 (2005) 1015–1047.
[12] H. Lubatschowski, G. Maatz, A. Heisterkamp, U. Hetzel, W. Drommer, H. Welling, W. Ertmer, Graefe Arch. Clin. Exp. Ophthalmol. 238 (2000) 33–39.
[13] E. Boulais, R. Lachaine, M. Meunier, Nano Lett. 12 (2012) 4763–4769.
[14] E.N. Glezer, C.B. Schaffer, N. Nishimura, E. Mazur, Opt. Lett. 22 (1997) 1817–1819.
[15] C.L. Arnold, A. Heisterkamp, H. Lubatschowski, J. Laser Micro/Nanoeng. 4 (2009) 39–44.
[16] R. Lausten, P. Balling, Appl. Phys. Lett. 79 (2001) 884–886.
[17] C. Sarpe, J. Köhler, T. Winkler, M. Wollenhaupt, T. Baumert, New J. Phys. 14 (2012) 75021.
[18] P. Balling, J. Schou, Rep. Prog. Phys. 76 (2013) 36502.
[19] J. Köhler, M. Wollenhaupt, T. Bayer, C. Sarpe, T. Baumert, Opt. Express 19 (2011) 11638–11653.
[20] M. Born, E. Wolf, Principles of Optics-Electromagnetic Theory of Propagation, Interference and Diffraction of Light, Cambridge University Press, 1999.
[21] N. Linz, S. Freidank, X.-X. Liang, H. Vogelmann, T. Trickl, A. Vogel, Phys. Rev. B 91 (2015) 134114.
[22] P. Audebert, P. Daguzan, A. Dos Santos, J.C. Gauthier, J.P. Geindre, S. Guizard, G. Hamoniaux, K. Krastev, P. Martin, G. Petite, A. Antonetti, Phys. Rev. Lett. 73 (1994) 1990–1993.
[23] S. Guizard, A. Semerok, J. Gaudin, M. Hashida, P. Martin, F. Quéré, Appl. Surf. Sci. 186 (2002) 364–368.
[24] N. Bloembergen, IEEE J. Quantum Electron. QE-10 (1974) 375–386.
[25] V.V. Temnov, K. Sokolowski-Tinten, P. Zhou, A. El-Khamhawy, D. von der Linde, Phys. Rev. Lett. 97 (2006) 237403.
[26] S.S. Mao, F. Quéré, S. Guizard, X. Mao, R.E. Russo, G. Petite, P. Martin, Appl. Phys. A 79 (2004) 1695–1709.
[27] P.K. Kennedy, IEEE J. Quantum Electron. 31 (1995) 2241–2249.
[28] E.G. Gamaly, Phys. Rep. 508 (2011) 91–243.
[29] A. Kaiser, B. Rethfeld, M. Vicanek, G. Simon, Phys. Rev. B 61 (2000) 11437–11450.
[30] B.H. Christensen, P. Balling, Phys. Rev. B 79 (2009) 155424.
[31] M. Daimon, A. Masumura, Appl. Opt. 46 (2007) 3811.
[32] J. Siegel, J. Solis, in: R. Osellame, G. Cerullo, R. Ramponi (Eds.), Femtosecond Laser Micromachining, Springer, Berlin, Heidelberg, 2012, pp. 19–41.
[33] K. Waedegaard, M. Frislev, P. Balling, Appl. Phys. A: Mater. Sci. Process. 110 (2013) 601–605.
[34] L. Jiang, H.-L. Tsai, J. Appl. Phys. 104 (2008) 93101.
[35] M. Wollenhaupt, A. Assion, T. Baumert, Springer Handbook of Lasers and Optics, Springer, 2012.
[36] R. Kammel, R. Ackermann, J. Thomas, J. Götte, S. Skupin, A. Tunnermann, S. Nolte, Light: Sci. Appl. 3 (2014) 1–8.
[37] C.A. Sacchi, J. Opt. Soc. Am. B 8 (1991) 337–345.
[38] F. Williams, S.P. Varma, S. Hillenius, J. Chem. Phys. 64 (1976) 1549–1554.
[39] C.G. Elles, A.E. Jailaubekov, R.A. Crowell, S.E. Bradforth, J. Chem. Phys. 125 (2006) 044515-1–044515-12.
[40] C.G. Elles, I.A. Shkrob, R.A. Crowell, S.E. Bradforth, J. Chem. Phys. 126 (2007), 164503–164503-8.
[41] C.B. Schaffer, N. Nishimura, E.N. Glezer, A.M.-T. Kim, E. Mazur, Opt. Express 10 (2002) 196–203.
[42] K.J. Wædegaard, D.B. Sandkamm, A. Mouskeftaras, S. Guizard, P. Balling, Europhys. Lett. 105 (2014) 47001.
[43] M. Wollenhaupt, L. Englert, A. Horn, T. Baumert, Proc. SPIE 7600 (2010), 76000X–76000X-11.
[44] A. Couairon, A. Mysyrowicz, Phys. Rep. 441 (2007) 47–189.
[45] J.R. Gulley, S.W. Winkler, W.M. Dennis, C.M. Liebig, R. Stoian, Phys. Rev. A 85 (2012) 13808.
[46] S.W. Winkler, I.M. Burakov, R. Stoian, N.M. Bulgakova, A. Husakou, A. Mermillod-Blondin, A. Rosenfeld, D. Ashkenasi, I.V. Hertel, Appl. Phys. A 84 (2006) 413–422.
[47] Z.W. Wilkes, S. Varma, Y.-H. Chen, H.M. Milchberg, T.G. Jones, A. Ting, Appl. Phys. Lett. 94 (2009) 211102.
[48] N.M. Bulgakova, V.P. Zhukov, Y.P. Meshcheryakov, L. Gemini, J. Brajer, D. Rostohar, T. Mocek, J. Opt. Soc. Am. B 31 (2014) C8–C14.